Editors' Suggestion

Controlling Rydberg Excitations Using Ion-Core Transitions in Alkaline-Earth Atom-Tweezer Arrays

Alex P. Burgers,[1] Shuo Ma,[1,2] Sam Saskin,[1,2] Jack Wilson,[1] Miguel A. Alarcón,[3,4] Chris H. Greene,[3,4] and Jeff D. Thompson[1,*]

[1] *Department of Electrical and Computer Engineering, Princeton University, Princeton, New Jersey 08544, USA*
[2] *Department of Physics, Princeton University, Princeton, New Jersey 08544, USA*
[3] *Department of Physics and Astronomy, Purdue University, West Lafayette, Indiana 47907, USA*
[4] *Purdue Quantum Science and Engineering Institute, Purdue University, West Lafayette, Indiana 47907, USA*

(Received 18 October 2021; revised 27 January 2022; accepted 24 March 2022; published 6 May 2022; corrected 24 August 2022)

Scalable local control over gate operations is an outstanding challenge in the field of quantum computing and programmable quantum simulation with Rydberg-atom arrays. One approach is to use a global field to excite atoms to the Rydberg state and tune individual atoms in and out of resonance via local light shifts. In this work, we point out that photon-scattering errors from light shifts can be significantly reduced if the light shift is applied to the Rydberg state instead of the ground state, which can be realized in Rydberg states of alkaline-earth atoms using optical transitions in the ion core. As a proof of concept, we experimentally demonstrate global control of Rydberg excitations in an Yb optical-tweezer array via light shifts induced by a laser tuned near the Yb^+ $6s \rightarrow 6p_{1/2}$ transition. We also perform detailed spectroscopy of the induced light shift and scattering rates of the $6sns\ ^3S_1$ Rydberg states and reveal the existence of satellite lines where losses from autoionization are strongly suppressed. This work can be readily extended to implement local gate operations in Rydberg-atom arrays.

DOI: 10.1103/PRXQuantum.3.020326

I. OVERVIEW

Neutral atoms trapped in reconfigurable optical-tweezer arrays are a leading platform for quantum computation and quantum simulation. Key features of this approach are bottom-up control afforded by optical-tweezer technology [1–3] and strong controllable interactions via Rydberg excitations [4,5]. In recent years, this platform has been used to microscopically probe the properties and dynamics of quantum phase transitions [6–9], to generate and probe large-scale entangled states [10,11], and to implement high-fidelity gate operations in multiqubit arrays [12–14].

An outstanding challenge in the field of Rydberg-atom arrays is scalable local addressing of gate operations, especially for multiqubit gates involving excitation to the Rydberg state. The generation of rapidly switchable, reconfigurable, and focused Rydberg excitation beams across an atomic array is demanding for optical modulators, as the intensity, pointing, and frequency of these beams must be tightly regulated [15]. This challenge is exacerbated for the wavelengths needed for single-photon Rydberg excitation (near or below 300 nm [14,16,17]), for which very few optical materials are transparent.

An alternative approach is to apply local light shifts using nonresonant control beams, to tune the ground-to-Rydberg ($|g\rangle \rightarrow |r\rangle$) transition on individual sites out of resonance with a global Rydberg excitation beam [Fig. 1(a)]. In addition to relaxing the stability requirements for the addressing beam, this approach also readily scales to parallel-gate implementation [12], an important consideration for fault-tolerant quantum computing [18]. Local control with light shifts has been demonstrated with Rydberg tweezer arrays [10,19–21] and with microwave transitions in optical lattices [22,23]. In the particular case of implementation of Rydberg-blockade gates on qubits encoded in hyperfine atomic levels, the local light shift determines which atoms participate in the gate and which are spectators [19]. To avoid spurious interactions with spectator atoms, the magnitude of the light shift must be much larger than the global Rydberg Rabi frequency. At the same time, photon scattering from local addressing beams must be suppressed to avoid gate errors. Consequently, to achieve high-fidelity operation, these conditions must be balanced, requiring

*jdthompson@princeton.edu

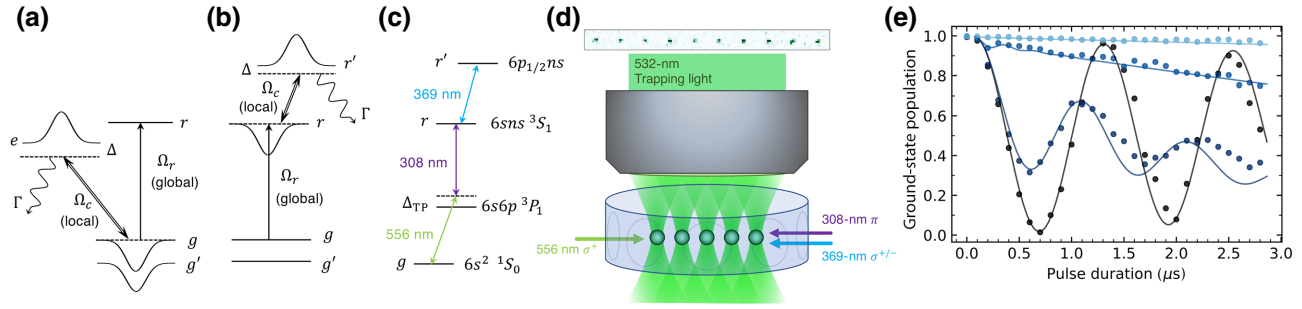

FIG. 1. (a) In the conventional approach to local control with light shifts, the $|g\rangle \rightarrow |r\rangle$ transition is detuned via a shift on $|g\rangle$ generated by driving the $|g\rangle \rightarrow |e\rangle$ transition, using a control field with Rabi frequency Ω_c and detuning Δ, where $|e\rangle$ has linewidth Γ. A second ground state $|g'\rangle$ used to encode a qubit will typically also experience a light shift. (b) In the approach presented here, the light shift is generated with a control field tuned near a transition from $|r\rangle$ to another highly excited state, $|r'\rangle$, which leaves the ground states unshifted. (c) Levels in ^{174}Yb relevant to this work: $|g\rangle = {}^1S_0$ is coupled to the Rydberg state $|r\rangle = 6sns\,{}^3S_1$ by a two-photon transition through $^3P_1$ with intermediate detuning $\Delta_{TP} = 2\pi \times 40$ MHz. The control field drives the $6sns \rightarrow 6p_{1/2}ns$ transition. (d) A schematic of the experiment, indicating the propagation direction and polarization of the driving fields shown in (c). The Rydberg and control beams are focused to approximately 15 μm $1/e^2$ radius at the position of the atoms. (e) Rabi oscillations between $|g\rangle$ and $|r\rangle$ (black) are suppressed by the addition of increasing control-beam intensities (black to blue: $I_c = 0, 15, 90, 600$ W/cm^2). The solid lines show the result of a numerical simulation.

both a large detuning and large intensity of the control beam.

Here, we point out that the scattering error can be significantly reduced if the control beam only couples to the Rydberg state, $|r\rangle$ [Fig. 1(b)]. In this case, the scattering errors occur primarily from $|r\rangle$ but the population of this state is suppressed for atoms illuminated by the control beam, which remain in the ground state. As a consequence, the control beam can be operated at much smaller detunings and lower powers.

Unfortunately, in alkali atoms such as Rb and Cs, there are no strong optical transitions connected to $|r\rangle$. In alkaline-earth atoms (AEAs) with two valence electrons, the situation is different: the Rydberg-electron orbits an optically active ion core, which has strong allowed transitions. The far off-resonance polarizability of these transitions has been used for trapping Yb [24] and Sr [25] Rydberg atoms, while the short lifetime (via autoionization decay) of core excited states has been used for efficient state detection in Sr atomic gases [26] and tweezer arrays [14].

In this work, we explore the use of these ion-core transitions to control Rydberg excitations in Yb (Fig. 1). We first quantify the control field intensity I_c needed to realize locally addressed operations with an error rate ϵ by shifting the ground states or the Rydberg states and find that scaling is improved from $I_c \propto 1/\epsilon^3$ to $I_c \propto 1/\epsilon^2$ in the latter case. We then experimentally demonstrate control of Rydberg excitations in an optical-tweezer array of ^{174}Yb atoms [24,27] using a light shift induced on the Rydberg state by a control beam tuned near the 369-nm $6s \rightarrow 6p_{1/2}$ transition in the Yb^+ ion core. We investigate the influence of the control beam on the $6sns\ {}^3S_1$ Rydberg states in detail and find that, near resonance, the light shift and autoionization scattering rate can be described by a two-level system model, consistent with the isolated-core-electron (ICE) approximation for doubly excited Rydberg states [28]. We then use the global control beam to switch *on* and *off* the excitation of both single atoms and high-fidelity Bell states [$\mathcal{F} > 0.948(12)$] in pairs of interacting atoms, using a control-beam intensity equivalent to only 1.3 μW in a diffraction-limited spot. Lastly, we observe that for larger control-beam detunings (comparable to the spacing between Rydberg levels), satellite features called "shake-up" lines [29,30] appear, giving rise to an additional suppression of the scattering rate without altering the light shift. We demonstrate an additional reduction in scattering errors from the control beam at these special detunings.

These proof-of-concept experiments demonstrate global control over Rydberg excitations from $|g\rangle \rightarrow |r\rangle$ and can be readily extended to locally controlled quantum gate operations. This extension requires two additional steps: focusing the 369-nm light down to single sites and introducing a second stable level $|g'\rangle$ to define a qubit. This could be the $^3P_0$ clock state in ^{174}Yb or an additional hyperfine state in an odd isotope such as ^{171}Yb. The latter approach has the advantage that the differential light shift on the qubit levels is extremely small, further relaxing the intensity-stability requirements for the control beam.

II. CONTROLLING GATES WITH AN ION-CORE LIGHT SHIFT

We first establish the theoretical scaling of the addressing fidelity with the intensity of the control light. We consider the following scenario: given a regular array of atoms with qubits encoded in hyperfine ground states [Fig. 1(a)],

we wish to apply an entangling Rydberg-blockade gate using a global Rydberg beam [12,31] (with Rabi frequency Ω_r) to a sparse subset of nearest-neighbor qubit pairs, while realizing no operation (up to single-qubit phases) on the remaining spectator qubits. Given a control beam that shifts the state $|g\rangle$ in the spectator atoms relative to $|r\rangle$ by an amount $\Delta_{LS} = \Omega_c^2/(4\Delta)$ and induces a scattering rate $\Gamma_{LS} = \Gamma\Omega_c^2/(4\Delta^2)$ [32] [see Fig. 1(a) for variable definitions], there are two dominant errors. The first is the probability for a spectator atom to be excited off resonantly to $|r\rangle$, $P_r \propto (\Omega_r/\Delta_{LS})^2$ and thereby blockade the intended gate, which results in an error probability $\epsilon_{\rm rot} \propto P_r$. The second is a photon-scattering error in the spectator atom, with a probability $\epsilon_{\rm sc} \propto \Gamma_{LS} t_g$ ($t_g \propto 2\pi/\Omega_r$ is the gate duration). We note that the former error is improved with larger control-field intensity, while the latter gets worse, resulting in a minimum total error that can only be reduced by increasing Δ.

There is also an intrinsic gate error on the qubits participating in the gate, resulting from the finite lifetime of the Rydberg state, $\epsilon \propto t_g\Gamma_r = 2\pi\Gamma_r/\Omega_r$, where Γ_r is the decay rate of $|r\rangle$. A natural condition is that the addressing errors should be comparable to the intrinsic error, $\epsilon_{\rm rot} + \epsilon_{\rm sc} = \epsilon$. The minimum detuning and control intensity needed to realize this are $\tilde{\Delta} \propto \Gamma/\epsilon^{3/2}$ and $\tilde{I}_c \propto |\tilde{\Omega}_c|^2 \propto \Gamma\Gamma_r/\epsilon^3$.

If the light shift is applied on the state $|r\rangle$ by coupling to another state $|r'\rangle$ [Fig. 1(b)], the spectator-qubit error probability $\epsilon_{\rm rot}$ is the same but now the scattering error is strongly suppressed, since only the $|r\rangle$ state experiences loss. In this case, $\epsilon_{\rm sc} \propto \Gamma_{LS} t_g P_r$, with $P_r \propto \epsilon_{\rm rot}$ as before. Since $\epsilon_{\rm rot} \propto \Omega_c^{-4}$ and $\Gamma_{LS} \propto \Omega_c^2$, both errors now decrease monotonically with increasing control power. The condition $\epsilon_{\rm rot} + \epsilon_{\rm sc} = \epsilon$ can be satisfied with $\tilde{\Delta} \propto \Gamma/\sqrt{\epsilon}$, and $\tilde{I}_c \propto |\tilde{\Omega}_c|^2 \propto \Gamma\Gamma_r/\epsilon^2$. This is a slower increase in power with ϵ than for ground-state shifting, which can result in a very significant advantage for high fidelity gates.

III. EXPERIMENTAL DEMONSTRATION

We now turn to an experimental demonstration of controlling Rydberg excitations by shifting $|r\rangle$ using an ion-core transition. Our experiment begins by creating a one-dimensional defect-free array [2,3] of ten ^{174}Yb atoms in the $^1S_0$ ground state $|g\rangle$. This state is coupled to the $6s75s\,^3S_1$ ($m_J = +1$) Rydberg state $|r\rangle$ in a two-photon process via the $^3P_1$ state [Fig. 1(c)], with an intermediate state detuning of $\Delta_{TP} = 2\pi \times 40$ MHz and two-photon Rabi frequency $\Omega_r = 2\pi \times 0.7$ MHz. The 369-nm control beam with intensity I_c is copropagating with the Rydberg lasers and is stabilized near the $|r\rangle \rightarrow |r'\rangle$ transition using a wave meter with 60-MHz accuracy. At the end of the experiment, any population in $|r\rangle$ is removed using a second pulse of the 369-nm beam, at full power, before detecting the remaining atoms in $|g\rangle$ [14]. Without this pulse, approximately 20% of atoms in $|r\rangle$ return to $|g\rangle$ before detection as they are trapped [24].

The essential result is illustrated in Fig. 1(e). In an array of atoms with large spacing (i.e., negligible interactions), we observe Rabi oscillations between $|g\rangle$ and $|r\rangle$ with a high visibility in the absence of the control beam. Applying the control beam with successively higher intensities, these oscillations become damped and eventually cease, with the atoms remaining in the initial state $|g\rangle$. The control light is detuned by $\Delta/(2\pi) = -5$ GHz from the $|r\rangle \rightarrow |r'\rangle$ transition. The decay from $|r'\rangle$ is predominantly via autoionization, which leads to atom loss. Therefore, the high survival probability in $|g\rangle$ directly illustrates that the rate of these scattering events is small. We note that only modest control-beam power is required: the highest I_c, 600 W/cm^2, is equivalent to only 1.3 μW in a diffraction-limited spot with $w_0 = \lambda$.

To better understand and quantitatively model the properties of the $|r\rangle \rightarrow |r'\rangle$ transition, we measure the light shift and scattering rate of $|r\rangle$ in the presence of the 369-nm control beam with variable detuning from the Yb$^+$ resonance at $f_+ = 811.291\,50(40)$ THz [Fig. 2(a)] [33]. The light shift, Δ_{LS}, is extracted from the resonance shift of the $|g\rangle \rightarrow |r\rangle$ transition, while the scattering rate, Γ_{LS}, is measured from the lifetime of $|r\rangle$ [24], assuming that most scattering events result in autoionization

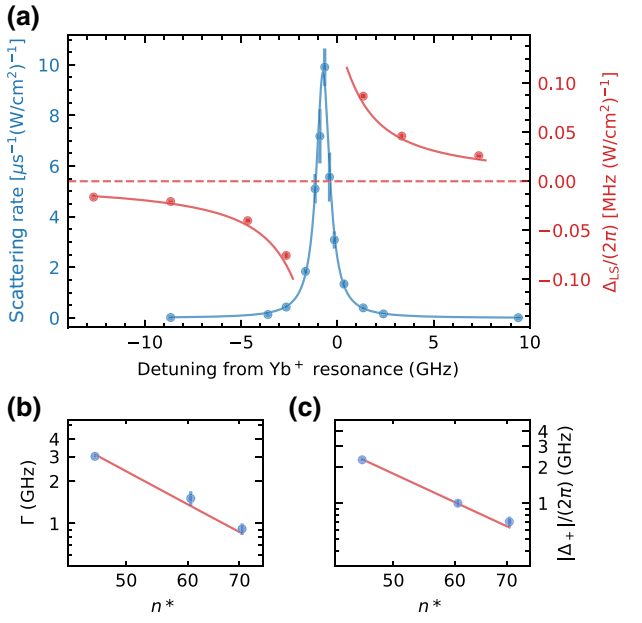

FIG. 2. (a) $\Delta_{LS}/(2\pi)$ (red) and Γ_{LS} (blue) for the $6s75s\ ^3S_1$ state, as a function of the control-beam detuning from the Yb$^+$ $6s \rightarrow 6p_{1/2}$ transition frequency, f_+. The lines are fits to the expressions in the text. (b) The extracted linewidth, Γ and (c) center frequency offset Δ_+ as a function of $n^* = n - \delta$ with $\delta = 4.439$ [24]. A fit to $(n^*)^{-3}$ is included from which we extract the following: $\Gamma(n^*) = 2\pi \times 2.9 \times 10^{14}\ \mathrm{s}^{-1}/n^{*3}$ and $|\Delta_+(n^*)|/(2\pi) = 2.2 \times 10^{14}\ \mathrm{Hz}/n^{*3}$.

of the atom. These measurements are performed over a range of powers, with linear scaling observed in all cases.

The data are well described by a two-level system model, $\Delta_{LS} = \Omega_c^2\Delta/(4\Delta^2 + \Gamma^2)$ and $\Gamma_{LS} = \Gamma\Omega_c^2/(4\Delta^2 + \Gamma^2)$ [34]. From a fit to the scattering rate, Γ_{LS}, we extract the parameters $\Delta = f - (f_+ + \Delta_+)$, $\Gamma = 2\pi \times 0.92(3)$ GHz and a dipole moment $d = \hbar\Omega_c/E_c = 1.46(2)ea_0$ (where E_c is the electric field strength of the control beam). The transition is centered at a frequency $\Delta_+/(2\pi) = -0.73(7)$ GHz below the Yb^+ transition frequency. The dipole moment is also consistent with that of the bare Yb^+ $6p_{1/2}$ transition [35], taking into account a Clebsch-Gordan coefficient for the $\sigma^{+/-}$ polarization of the laser. The same model describes the light shift Δ_{LS}, although the magnitude of the light shift is approximately 30% smaller than would be predicted from the parameters above. We repeat these measurements at $n = 50$ and 65 to understand the scaling properties of these parameters. Both $|\Delta_+|$ and Γ scale as $1/n^{*3}$, proportional to the Rydberg-electron probability density at the Yb^+ ion core [Figs. 2(b) and 2(c)] [30].

We now study the effectiveness of the control beam at modulating Rydberg excitation induced by Ω_r in the case of isolated noninteracting atoms [Fig. 3(a)]. To do this, we apply Ω_r for a time $t_g = \pi/\Omega_r \approx 700$ ns (π pulse), while varying the control-beam intensity I_c. The control-beam detuning is fixed at $\Delta/(2\pi) = -5$ GHz. In this experiment, the atoms are spaced by $d = 21$ μm, such that the van der Waals interaction is negligible compared to Ω_r. In the absence of the control beam, around 97% of the ground-state population is transferred to $|r\rangle$, limited by residual technical noise, Doppler shifts and photon scattering. However, at the maximum I_c, the Rydberg excitation is suppressed and the atoms remain in $|g\rangle$ with 98.7(2)% probability. The data are in excellent agreement with a numerical simulation based on parameters extracted from Fig. 2(a) (described in Appendix D).

Next, we demonstrate control over coherent excitations in the Rydberg-blockade regime using an array of atom pairs (dimers) [Fig. 3(b)]. The intradimer spacing is 3.15 μm, for which we estimate a blockade strength $V \gg 100$ MHz [36]. We apply Ω_r for a time $t_g = \pi/(\sqrt{2}\Omega_r) \approx 500$ ns, which drives a π pulse on the blockaded transition $|gg\rangle \rightarrow |\phi^+\rangle = (|gr\rangle + |rg\rangle)/\sqrt{2}$. When I_c is small, we extract a lower bound of the state fidelity (with respect to the Bell state $|\phi^+\rangle$) of $\mathcal{F}_{\phi^+} > 0.948(12)$, based on a lower bound on the state purity after a $2t_g$ pulse [14] (see Appendix C). However, at the maximum I_c, the oscillations are highly suppressed and the fidelity with the starting state is $\mathcal{F}_{gg} = 0.978(3)$.

Lastly, we study the scattering rate and light shift over a broader range of control-beam detunings. Near the transition to other Rydberg states, such as $6s75s \rightarrow 6p_{1/2}74s$ ($\Delta/(2\pi) \approx -19$ GHz below the transition to $6p_{1/2}75s$), the scattering rate shows sharp Fano-like features [Fig. 4(a)] known as "shake-up" resonances [29,30]. These features arise from zeros in the overlap integral of the Rydberg-electron wave function in the initial and final states [37] and can be reproduced with a multichannel-quantum-defect-theory (MQDT) model (Appendix B). Experimentally, we observe a dip in the scattering rate that is a factor of 34 below the value predicted by the two-level model for Γ_{LS}.

Importantly, the light shift does not show any significantly irregular behavior near the shake-up resonance. The MQDT model predicts a small feature in the light shift (Appendix B) that deviates from the two-level system description by approximately 2% at these detunings. Therefore, operating the control laser at a detuning corresponding to the scattering minimum ($\Delta_{\min}$) is beneficial, reducing ϵ_{sc} or allowing the same total addressing error $\epsilon_{rot} + \epsilon_{sc}$ to be realized with less power. We experimentally demonstrate the reduction in ϵ_{sc} by simultaneously applying Ω_r and the control light for a long duration ($t \approx 7\pi/\Omega_r$), at three detunings near $\Delta_{\min}$ [Fig. 4(b)]. The light shift ($\Delta_{LS}/(2\pi) \approx 5.8 - 4.6$ MHz) suppresses coherent oscillations to approximately 1% for each detuning.

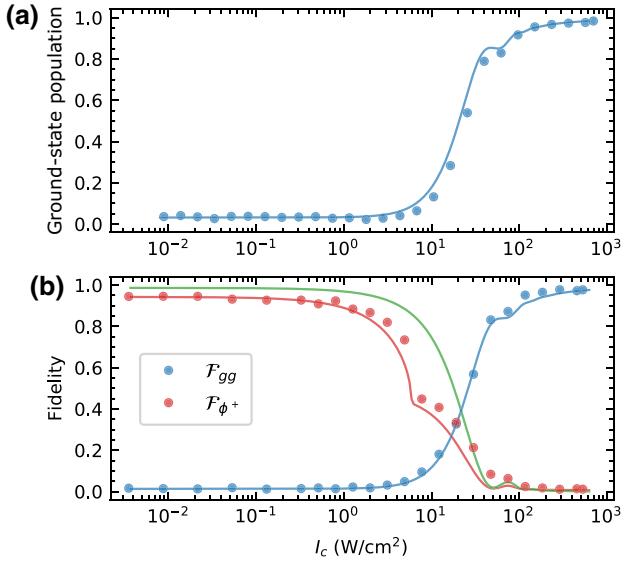

FIG. 3. (a) The probability of finding an atom in $|g\rangle$ after an attempted π pulse to $|r\rangle$, for varying control intensities I_c with $\Delta/(2\pi) = -5$ GHz. At high intensities, the population transfer is strongly suppressed and 98.7(2)% of the atoms remain in $|g\rangle$. (b) The final-state fidelity with $|\phi^+\rangle$ (red points, experimental lower bound) and $|gg\rangle$ (blue) after a π pulse in an array of dimers with a strong intradimer Rydberg blockade. The control beam switches the final state from having $> 0.948(12)$ fidelity with $|\phi^+\rangle$, to 0.978(3) fidelity with $|gg\rangle$. The curves show simulations of the same quantities using parameters from Fig. 2(a) and adding phenomenological dephasing and detection errors. The green curve shows the exact fidelity $\mathcal{F}_{\phi^+}$, while the red curve shows the experimentally measurable lower bound on $\mathcal{F}_{\phi^+}$.

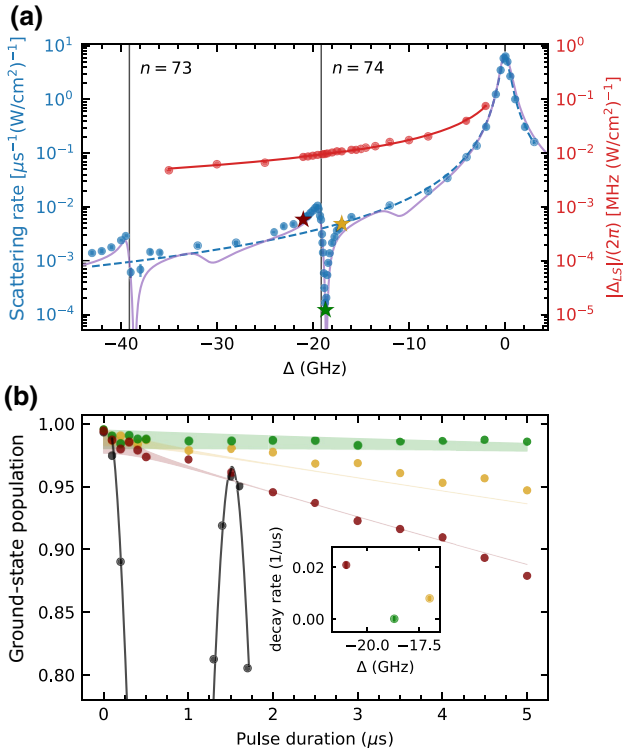

FIG. 4. (a) $|\Delta_{LS}|/(2\pi)$ (red) and Γ_{LS} (blue) for the $6s75s\ ^3S_1$ state, as in Fig. 2 but over a broader range of detunings with a fit of Γ_{LS} (blue dashed line) and a MQDT model (purple line) of the autoionization spectrum described in Appendix B. The positions of the $6p_{1/2}ns$ states (black lines) and the detuning that minimizes the scattering rate $\Delta_{\min}/(2\pi) = -18.7$ GHz (green star) are indicated. (b) Rabi oscillations to $|r\rangle$ (black, $I_c = 0$) are strongly suppressed by applying the control field at detunings near $\Delta_{\min}$ [the colors correspond to the starred points in (a)] and show good agreement with simulation (solid lines). We find that population decay (inset) from autoionization while light shifting the Rydberg state off resonance is suppressed below our experimental resolution when $\Delta = \Delta_{\min}$.

However, there is gradual population loss from ϵ_{sc} that is linear in Γ_{LS}. At $\Delta_{\min}$, we find that the loss during the 5 μs duration of the experiment is too small to observe. The behavior agrees with a master-equation simulation, where the shake-up resonance is incorporated as a reduction in Γ to match the experimentally measured Γ_{LS} at each of the starred detunings in Fig. 4(a).

IV. DISCUSSION

We now revisit the comparison of ground-state and excited-state shifting. Given the scaling relationships derived above, the power required to control operations with error ϵ using excited-state shifting, P_e, is related to the power for ground-state shifting, P_g, by $P_e/P_g = (d_g/d_e)^2(w_e/w_g)^2(\Gamma_e/\Gamma_g)\epsilon$, where d is the dipole moment, w is the beam waist (which we set equal to the transition wavelength, λ) and Γ is the linewidth. Comparing the approach in this work to ground-state shifting on the Rb D_2 line, as an example, we find that this expression reduces to $P_e/P_g \approx 55\epsilon$, which can alternately be expressed as a 18-fold reduction in power for an ambitious but reasonable future target of $\epsilon = 0.001$ [using $\Gamma_g/(2\pi) = 6$ MHz, $\lambda_g = 780$ nm, and $d_g = 1.99\ ea_0$, relevant for qubits in $m_F = 0$ states in Rb [38]]. We note that the required power for Yb can be reduced even further by exploiting the autoionization zeros in Fig. 4(a) (yielding a 34-fold reduction in scattering rate at certain detunings) or moving to higher n to decrease the autoionizing transition linewidth. Therefore, we predict that at least a 100-fold reduction in addressing power for gates with $\epsilon = 0.001$ is achievable. We also note that shifting Rydberg states via coupling to low-lying states [20] does not compare favorably to using autoionizing transitions: even though the scaling of the power with ϵ is the same and the transition linewidths can be narrower, this is offset by the significantly smaller dipole matrix elements (e.g., $d = 0.01\ ea_0$ for Rb $5p_{3/2} \rightarrow 60s_{1/2}$ [39]).

In conclusion, we demonstrate that a light shift of the Rydberg states using a core-electron transition can be used to control Rydberg excitations in an optical-tweezer array. In contrast to applying a light shift on the ground state, shifting the Rydberg state reduces the laser-power requirements to achieve a given error rate from photon scattering or off-target excitation. This demonstration is carried out with a global control laser; however, the main application of this result will be with locally addressed control fields and using the ^{171}Yb isotope with qubits encoded in the nuclear-spin sublevels of the $J = 0$ $^1S_0$ or $^3P_0$ states. In particular, this approach can be used to control single-photon excitation from $^3P_0$, which has the potential to realize very high-fidelity operations [14] but for which local addressing is challenging because of the short optical wavelength (302 nm). We note that local addressing using light near the Yb^+ transition has been demonstrated in ion=trap quantum computers [40].

ACKNOWLEDGMENTS

We acknowledge helpful conversations with Dolev Bluvstein. A.P.B., S.M., S.S., J.W., and J.D.T. were supported by the U.S. Army Research Office (ARO) Presidential Early Career Award for Scientists and Engineers (PECASE) (W911NF-18-10215), the Office of Naval Research (ONR) (N00014-20-1-2426), the Defense Advanced Research Projects Agency (DARPA) Optimization with Noisy Intermediate-Scale Quantum Devices (ONISQ) program (W911NF-20-10021), and the Sloan Foundation. S.S. was additionally supported by an ARO QuaGCR fellowship. M.A.A. and C.H.G. are supported in part by the Air Force Office of Scientific Research

(AFOSR) Multidisciplinary Research Program of the University Research Initiative (MURI), under Grant No. FA9550-20-1-0323.

APPENDIX A: EXPERIMENTAL METHODS

Our experimental apparatus has previously been described in Ref. [27]. We begin each experiment by loading ^{174}Yb atoms in a 532-nm tweezer array from a three-dimensional magneto-optical trap (MOT) on the $^1S_0$-to-$^3P_1$ transition. We generate the tweezer array using a pair of crossed acousto-optic deflectors (AODs) with multiple-input radio frequency (RF) tones from an arbitrary waveform generator (AWG) (Spectrum Instrumentation M4i.6622-x8). The diffracted light is projected into the chamber using a 0.6-NA objective (Special Optics). We image atoms in the tweezers and rearrange the atoms into a desired geometry by adjusting the RF tones on the AWG [2,3].

We excite atoms to the $6s75s\ ^3S_1$ Rydberg state via a two-photon transition [Fig. 1(c)] through $^3P_1$ ($m_J = 1$) with intermediate detuning $\Delta_{TP} = 2\pi \times 40$ MHz. We achieve a two-photon Rabi frequency of $\Omega_r = 2\pi \times 0.7$ MHz. The Rydberg excitation is driven by two lasers, one driving $^1S_0 \rightarrow {}^3P_1$ (556 nm, green) and the other driving $^3P_1 \rightarrow 6s75s\ ^3S_1$ (308 nm, UV). The green light is created via sum-frequency generation in a periodically poled lithium niobate (PPLN) crystal using a 1560-nm erbium-doped fiber amplifier (NKT Photonics) and a titanium sapphire laser (M Squared Solstis) at 862 nm. The UV light is created by frequency doubling 616-nm (orange) light that is generated using the same SFG process as the green light. The green and orange frequencies are stabilized to a high-finesse cavity (Stable Laser Systems). The 369-nm autoionization laser is a tunable diode laser (Toptica DL Pro) locked to a wave meter (High Finesse WS-7) with 60-MHz accuracy. During Rydberg excitation, the traps are turned off to avoid light shifts.

In order to measure the scattering rate from the autoionization transition, we first excite an array of atoms (with large separation, $d = 21$ μm) to the Rydberg state with a π pulse. This is followed by an autoionization pulse of variable duration and a second Rydberg π pulse that returns any atoms in the initially populated Rydberg state back to the ground state, where they are imaged. To extract the scattering rate, we measure the survival probability of atoms for the above sequence as a function of the autoionization-pulse duration and fit to an exponential decay [Figs. 2(a) and 4(a)]. The autoionization spectrum is obtained by repeating this process for different autoionization laser frequencies. We are able to measure the autoionization rate most accurately when it is between 100 ns and 10 μs. Therefore, we adjust the laser power for each frequency range to keep the autoionization rate in this range. We verify that the loss rate is linear in the power over a wide range at several different frequencies.

To measure the light shift, we perform spectroscopy of the Rydberg transition while illuminating the atoms with the control beam. Given the available laser power, we typically observe shifts of approximately 10–20 MHz, which are easily resolved.

For both quantities, we report intensity-normalized values to facilitate comparison across widely different detunings. These are based on a measured beam waist of 15 μm ($1/e^2$ radius). The beam waist at the position of the atoms is determined by observing the scattering rate as the beam is scanned, with the beam deflection monitored on a CCD camera outside of the vacuum chamber.

All experiments in the paper, other than the one reported in Fig. 3(b), are performed in tweezers with sufficiently large separation that interactions are negligible, typically $d = 21$ μm. In Fig. 3(b), the spacing within a dimer is 3.15 μm, while the spacing between dimers is 21 μm.

APPENDIX B: MULTICHANNEL QUANTUM DEFECT THEORY

In order to describe the autoionization process, we propose a five-channel model that aims to fit the spectrum by finding the MQDT parameters. The control laser couples to odd-parity $6p_{1/2}nl$ states with both $J' = 0$ and $J' = 1$. Under the assumption that photoionization occurs via an ICE process, the odd $J' = 2$ symmetry is not accessible for final Rydberg states attached to the $6p_{1/2}$ threshold. Omitting the open f shell channels that are suspected to be irrelevant, there are in total 18 channels, from which five correspond to $J' = 0$ and 13 correspond to $J' = 1$.

The simplest semirealistic model includes only a single open channel (as proposed for Ba in Ref. [41]) and only the $6p_{1/2}$ closed channels, which results in a total of five channels: two for $J' = 0$ and three for $J' = 1$ (Table I). The latter restriction is justified by the form of the dipole-matrix elements in the ICE, which involves the overlap between the radial wave functions in the closed channels.

TABLE I. The five-channel model with a single open channel on each symmetry. Here, J is the total angular momentum and j is the jj-coupled channel index. The closed channel principal quantum is denoted by n and is replaced by ϵ in the open channel case to represent its continuous kinetic energy.

$J = 0$		$J = 1$	
$j = 1$	$6s_{1/2}\epsilon p_{1/2}$	$j = 1$	$6s_{1/2}\epsilon p_{1/2}$
$j = 2$	$6p_{1/2}ns_{1/2}$	$j = 2$	$6p_{1/2}ns_{1/2}$
		$j = 3$	$6p_{1/2}nd_{3/2}$

TABLE II. The $\mu^J_{n,m}$ matrix elements for the two different symmetries corresponding to the fit in Fig 4. The superscript indicates the total J value and the subscripts indicate channel indices.

$\mu^0_{1,1}$	$\mu^0_{1,2}$	$\mu^0_{2,2}$			
$0.009(117)^*$	$0.171(22)$	$-0.483(14)^\dagger$			
$\mu^1_{1,1}$	$\mu^1_{1,2}$	$\mu^1_{1,3}$	$\mu^1_{2,2}$	$\mu^1_{2,3}$	$\mu^1_{3,3}$
$0.04(21)^*$	$-1.38(1)$	$0.04(13)^*$	$-0.135(8)^\dagger$	$-0.742(15)$	$0.10(17)^*$

* Consistent with zero.
† For these parameters, we do not have enough data to determine which peak is $J = 0$ and which is $J = 1$. An equally good fit can be generated with these assignments flipped; however, this would change the value of the other parameters.

The matrix K describing the short-range behavior is parametrized by the μ matrix [42], which we fit to the experimental data. This matrix is connected to the K matrix by $K = \tan(\pi\mu)$, where the tan is understood to be a matrix function.

To compare to the data, we compute the photoionization rate, R, as a function of the energy of the autoionizing atomic state $E = E_{75} + \omega$, where $E_{75} = 50\,421.0303\ \mathrm{cm}^{-1}$ is the energy of the $6s75s\ ^3S_1$ state [24] and ω is the control laser frequency. Adopting the notation of Ref. [43] for the outgoing wave function of the autoionizing state and the approximate overlap of the closed-channel functions [44], we find

$$R(E) = \frac{\pi}{2}\mathcal{E}_o^2\mathcal{D}^2_{6p_{1/2},6s_{1/2}}\left\{\frac{2\sin\left[\pi(\nu(E)-\nu_0)\right]\nu(E)^2\nu_0^2}{\sqrt{6}\nu_0^{3/2}\pi(\nu(E)^2-\nu_0^2)}\right\}^2 \times\left[\left|Z_{21}^{J=1}(E)\right|^2+\left|Z_{21}^{J=0}(E)\right|^2\right]. \tag{B1}$$

Here, $\nu_0 = 70.561$ is the effective quantum number of the $6s75s\ ^3S_1$ state with respect to the $6s_{1/2}$ threshold [24] and $\nu(E) = \sqrt{R_{\mathrm{Yb}}/(I_{6p_{1/2}} - E)}$ is the effective quantum number of the final autoionizing state with respect to the $6p_{1/2}$ threshold, $I_{6p_{1/2}}$, with the Yb Rydberg constant $R_{\mathrm{Yb}} = R \times m_{\mathrm{Yb}}/(m_{\mathrm{Yb}} + m_e)$. $Z_{21}(E)$ is the coefficient of the closed-channel function in the incoming wave boundary condition wave function, as described in Ref. [43], and $\mathcal{D}_{6p_{1/2},6s_{1/2}} = 2.6829ea_0$ is the reduced matrix element of the electric dipole operator in the core states [45]. The μ matrix that produces the best agreement with the experimental photoionization spectrum [Fig. 4(a)] is given in Table II.

The counterintuitive structure of this spectrum is worth some explanation. Since the electric dipole matrix element for an ICE is proportional to the overlap between closed-channel functions and in this limited MQDT model all the closed channels are attached to the same threshold, the ionization rates vanish exactly when $\nu_0 - \nu(E)$ is an integer different from zero. This exact vanishing will not happen if closed channels attached to the $6p_{3/2}$ channels are included, which may be the origin of the finite scattering rate at Δ_{min} observed in the experiment. This can also be modified by considering an initial wave function that includes amplitude in channels other than one attached to the $6s_{1/2}$ threshold. However, a complete MQDT model for the $^3S_1$ series in ^{174}Yb does not exist, as this series has only recently been observed for the first time [24].

The five-channel model has more parameters than can be accurately constrained by the experimental data. In order to fit both the satellite lines and the main feature, it proves necessary for the $J' = 0$ and $J' = 1$ ns resonances to be close in energy and overlapping, since the main feature at zero detuning does not suggest a composite peak. However, their relative energy ordering and widths are not strongly constrained by the current experimental data, which does not distinguish these symmetries. Similarly, the small outlying feature in the fit at detuning $\Delta/(2\pi) \approx -11$ GHz and $\Delta/(2\pi) \approx -31$ GHz comes from the zero of a Fano resonance [46] in the $J' = 1$ states. This feature is not observed in the sparsely sampled data in this detuning range and could, in fact, lie elsewhere. The model should be understood as an exemplary MQDT analysis, showing that the salient features of the data including the Fano-like peak around the satellite line can be reproduced with this approach. However, because of the limited amount of data (i.e., focusing on a single principal quantum number) and the restriction of the model to a small number of channels, it does not represent a definitive MQDT analysis of this autoionizing series. The parameter landscape has a number of local minima and, as a result, the uncertainty in many parameters is large. Future work with a larger set of experimental data and a more comprehensive experimental model will help develop a complete understanding of this autoionizing Rydberg series.

We can also compute the light shift predicted by the MQDT model. Adapting formula 4.3-27 of Ref. [47] to the autoionizing states, we find the following energy shift:

$$\Delta E_{75} = -\frac{1}{4}\mathcal{E}_o^2\mathcal{D}^2_{6p_{1/2},6s_{1/2}}\left(P\int\left\{\frac{2\sin\left[\pi(\nu(E)-\nu_0)\right]\nu(E)^2\nu_0^2}{\sqrt{6}\nu_0^{3/2}\pi(\nu(E)^2-\nu_0^2)}\right\}^2\left[|Z_{21}^{J=1}(E)|^2+|Z_{21}^{J=0}(E)|^2\right]\frac{1}{E-E_{75}-\omega}dE\right.$$
$$\left.+\,i\pi\left\{\frac{2\sin\left[\pi(\nu-\nu_0)\right]\nu^2\nu_0^2}{\sqrt{6}\nu_0^{3/2}\pi(\nu^2-\nu_0^2)}\right\}^2\left[|Z_{21}^{J=1}|^2+|Z_{21}^{J=0}|^2\right]\Big|_{E=E_{75}+\omega}\right), \tag{B2}$$

where P indicates the Cauchy principal value of the integral. The real part of ΔE_{75} gives the light shift, while the imaginary part reproduces the photoionization rate, in agreement with Eq. (B1), $R = -2\mathrm{Im}(\Delta E_{75})$. In Fig. 5, we plot the real part along with the light-shift data from Figs. 2(a) and 4(a) from the main text. The predicted light shift from the MQDT model is scaled by 0.7 to account for the 30% discrepancy between the predicted light shift from the scattering-rate model and the data, as is noted in the main text. The absence of a feature in the light shift near the satellite lines reflects the fact that the integral in Eq. (B2) derives most of its weight from the main resonance near zero detuning.

APPENDIX C: BELL-STATE FIDELITY MEASUREMENT

The Bell-state fidelity $\mathcal{F}_{\phi_+}$ is not directly accessible in the experiment without a local probe or the ability to perform single-qubit rotations on the $|g\rangle - |r\rangle$ subspace without the influence of the Rydberg blockade. Therefore, we quantify the fidelity with a lower bound using the method from Ref. [14], which is based on the state purity extracted from the populations at a time $2t_g$:

$$\mathcal{F}_{\phi_+}(t_g) > \frac{1}{2}\left[\rho_{gr,gr}(t_g)+\rho_{rg,rg}(t_g)\right]+\sqrt{\max\left\{0,\left[\sum_i \rho_{i,i}(2t_g)^2-1\right]/2+\rho_{gr,gr}(t_g)\rho_{rg,rg}(t_g)\right\}}. \tag{C1}$$

We use the two-atom basis populations (shown in Table III) averaged over the smallest three values of I_c to calculate the fidelity quoted in the text, $\mathcal{F}_{\phi_+} > 0.948(12)$. We note that these populations correspond to raw-measurement outcomes and are not corrected for any state preparation or measurement errors.

APPENDIX D: SIMULATIONS

Here, we provide details of the single- and two-atom simulations used to model the Rydberg-excitation dynamics in the presence of the control field, as presented in Fig. 3 of the main text.

1. Isolated atoms

For isolated noninteracting atoms, we solve the master equation for the following Hamiltonian:

$$H_1 = \frac{\Omega_r}{2}(\sigma^+_{r,g}+\sigma^-_{r,g})+\frac{\Omega_c}{2}(\sigma^+_{r,r'}+\sigma^-_{r,r'})-\Delta P_{r'}. \tag{D1}$$

We include an additional state, $|d\rangle$, in the Hilbert space to capture decay from the autoionizing state $|r'\rangle$, governed by the collapse operator $c_1 = \sqrt{\Gamma}\sigma^-_{r',d}$. We also include an additional collapse operator, $c_2 = \sqrt{\gamma_\mathrm{r}}\sigma^z_{g,r}$, to incorporate the observed dephasing of the Rabi oscillations at a phenomenological level. The dephasing rate, γ_r, is chosen to match the simulated ground-state population after a π pulse, $P_g(\pi/\Omega_r)$, to the experimental value when $I_c = 0$. We then compute $P_g(\pi/\Omega_r)$ as a function of I_c to generate the curve in Fig. 3(a).

To facilitate the comparison with the experiment, the simulated P_g is multiplied by the ground-state detection fidelity $F_g = 0.994$, extracted from an independent measurement with no Rydberg excitation.

2. Two-atom blockade

To model the Rydberg excitation dynamics in the presence of interactions, we extend our previous model into the following two-atom Hamiltonian:

$$H_2 = H_1\otimes\mathbb{1}+\mathbb{1}\otimes H_1+U_\mathrm{int}P_r\otimes P_r. \tag{D2}$$

We now include four collapse operators: $c_1 = \sqrt{\Gamma}\sigma^-_{r',d}\otimes\mathbb{1}$, $c_2 = \sqrt{\Gamma}\mathbb{1}\otimes\sigma^-_{r',d}$, $c_3 = \sqrt{\gamma_r}\sigma^z_{g,r}\otimes\mathbb{1}$, and $c_4 = \sqrt{\gamma_r}\mathbb{1}\otimes$

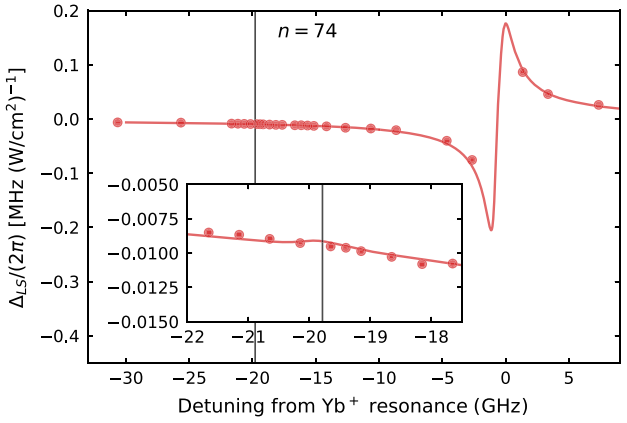

FIG. 5. The scaled light-shift curve using the MQDT-model parameters and Eq. B2 with data from the main text. Importantly, the MQDT model for the light shift does not predict a feature near the satellite lines ($n = 74$ indicated with a black line). The inset shows an enlargement of the light shift near the shake-up resonance, where the MQDT model predicts a minor structure, indicating that the light shift is almost entirely dominated by the main autoionization transition.

$\sigma^z_{g,r}$. In order to account for imperfect ground-state detection, we transform the simulated populations using the following matrix:

$$T_{(\mathrm{sim}\to\mathrm{exp})} = \begin{pmatrix} F_g^2 & 0 & 0 & 0 \\ F_g(1-F_g) & F_g & 0 & 0 \\ F_g(1-F_g) & 0 & F_g & 0 \\ (1-F_g)^2 & 1-F_g & 1-F_g & 1 \end{pmatrix}. \tag{D3}$$

We directly simulate the ground-state probability $P_{gg}(t_g)$ and the fidelity of the Bell state $\mathcal{F}_{\phi_+} = \mathrm{Tr}\left[\rho(t_g)\,|\phi_+\rangle\langle\phi_+|\right]$ after a pulse of duration $t_g = \pi/\sqrt{2}\Omega_r$, for various I_c [here, $\rho(t)$ is the two-atom density matrix at time t]. We also compute the fidelity lower bound from Eq. (C1) and plot this in Fig. 3(a). The good agreement with the measurement suggests that the observed infidelity is significantly limited by the lack of a direct entanglement probe.

Lastly, we note that these simulations treat the $|r\rangle \to |r'\rangle$ transition as a two-level system. However, as discussed above, the observed light shift and scattering rate on this transition are not self-consistently described by a single linewidth and dipole moment, with the apparent strength of the light shift being smaller by a factor of 0.7. To incorporate this into the simulation, we increase the linewidth by a factor of $1/0.7$ and scale the control intensity by 0.7. For values of $\Delta \gg \Gamma$, this accurately reproduces the experimentally measured Δ_{LS} and Γ_{LS}. Without this modification, the agreement between the simulation and experiment in Fig. 3(b) is considerably worse.

TABLE III. The two-atom basis populations for the lowest three values of I_c at t_g and $2t_g$ used to calculate the fidelity from Eq. C1.

	t_g	$2t_g$
$\rho_{gr,gr}$	0.487(8)	0.013(2)
$\rho_{rg,rg}$	0.494(8)	0.013(2)
$\rho_{rr,rr}$	0.005(1)	0.006(1)
$\rho_{gg,gg}$	0.014(2)	0.968(3)

[1] N. Schlosser, G. Reymond, I. Protsenko, and P. Grangier, Sub-Poissonian loading of single atoms in a microscopic dipole trap, Nature **411**, 1024 (2001).

[2] M. Endres, H. Bernien, A. Keesling, H. Levine, E. R. Anschuetz, A. Krajenbrink, C. Senko, V. Vuletic, M. Greiner, and M. D. Lukin, Atom-by-atom assembly of defect-free one-dimensional cold atom arrays, Science **354**, 3752 (2016).

[3] D. Barredo, S. de Léséleuc, V. Lienhard, T. Lahaye, and A. Browaeys, An atom-by-atom assembler of defect-free arbitrary two-dimensional atomic arrays, Science **354**, 1021 (2016).

[4] M. D. Lukin, M. Fleischhauer, R. Cote, L. M. Duan, D. Jaksch, J. I. Cirac, and P. Zoller, Dipole Blockade and Quantum Information Processing in Mesoscopic Atomic Ensembles, Phys. Rev. Lett. **87**, 037901 (2001).

[5] M. Saffman, T. G. Walker, and K. Mølmer, Quantum information with Rydberg atoms, Rev. Mod. Phys. **82**, 2313 (2010).

[6] H. Bernien, S. Schwartz, A. Keesling, H. Levine, A. Omran, H. Pichler, S. Choi, A. S. Zibrov, M. Endres, M. Greiner, V. Vuletić, and M. D. Lukin, Probing many-body dynamics on a 51-atom quantum simulator, Nature **551**, 579 (2017).

[7] S. de Léséleuc, V. Lienhard, P. Scholl, D. Barredo, S. Weber, N. Lang, H. P. Büchler, T. Lahaye, and A. Browaeys, Observation of a symmetry-protected topological phase of interacting bosons with Rydberg atoms, Science **365**, 775 (2019).

[8] P. Scholl, M. Schuler, H. J. Williams, A. A. Eberharter, D. Barredo, K.-N. Schymik, V. Lienhard, L.-P. Henry, T. C. Lang, T. Lahaye, A. M. Läuchli, and A. Browaeys, Quantum simulation of 2D antiferromagnets with hundreds of Rydberg atoms, Nature **595**, 233 (2021).

[9] S. Ebadi, T. T. Wang, H. Levine, A. Keesling, G. Semeghini, A. Omran, D. Bluvstein, R. Samajdar, H. Pichler, W. W. Ho, S. Choi, S. Sachdev, M. Greiner, V. Vuletić, and M. D. Lukin, Quantum phases of matter on a 256-atom programmable quantum simulator, Nature **595**, 227 (2021).

[10] A. Omran, H. Levine, A. Keesling, G. Semeghini, T. T. Wang, S. Ebadi, H. Bernien, A. S. Zibrov, H. Pichler, S. Choi, J. Cui, M. Rossignolo, P. Rembold, S. Montangero, T. Calarco, M. Endres, M. Greiner, V. Vuletić, and M. D. Lukin, Generation and manipulation of Schrödinger cat states in Rydberg atom arrays, Science **365**, 570 (2019).

[11] J. Choi, A. L. Shaw, I. S. Madjarov, X. Xie, J. P. Covey, J. S. Cotler, D. K. Mark, H.-Y. Huang, A. Kale, H. Pichler, F. G. S. L. Brandão, S. Choi, and M. Endres, Emergent

randomness and benchmarking from many-body quantum chaos (2021), ArXiv:2103.03535.

[12] H. Levine, A. Keesling, G. Semeghini, A. Omran, T. T. Wang, S. Ebadi, H. Bernien, M. Greiner, V. Vuletić, H. Pichler, and M. D. Lukin, Parallel Implementation of High-Fidelity Multiqubit Gates with Neutral Atoms, Phys. Rev. Lett. **123**, 170503 (2019).

[13] T. M. Graham, M. Kwon, B. Grinkemeyer, Z. Marra, X. Jiang, M. T. Lichtman, Y. Sun, M. Ebert, and M. Saffman, Rydberg-Mediated Entanglement in a Two-Dimensional Neutral Atom Qubit Array, Phys. Rev. Lett. **123**, 230501 (2019).

[14] I. S. Madjarov, J. P. Covey, A. L. Shaw, J. Choi, A. Kale, A. Cooper, H. Pichler, V. Schkolnik, J. R. Williams, and M. Endres, High-fidelity entanglement and detection of alkaline-earth Rydberg atoms, Nat. Phys. **16**, 857 (2020).

[15] C. Monroe and J. Kim, Scaling the ion trap quantum processor, Science **339**, 1164 (2013).

[16] P. Schauß, M. Cheneau, M. Endres, T. Fukuhara, S. Hild, A. Omran, T. Pohl, C. Gross, S. Kuhr, and I. Bloch, Observation of spatially ordered structures in a two-dimensional Rydberg gas, Nature **491**, 87 (2012).

[17] A. M. Hankin, Y.-Y. Jau, L. P. Parazzoli, C. W. Chou, D. J. Armstrong, A. J. Landahl, and G. W. Biedermann, Two-atom Rydberg blockade using direct 6*s* to *np* excitation, Phys. Rev. A **89**, 033416 (2014).

[18] J. Preskill, in *Introduction to Quantum Computation and Information* (World Scientific, 1998), p. 213.

[19] H. Labuhn, S. Ravets, D. Barredo, L. Béguin, F. Nogrette, T. Lahaye, and A. Browaeys, Single-atom addressing in microtraps for quantum-state engineering using Rydberg atoms, Phys. Rev. A **90**, 023415 (2014).

[20] S. de Léséleuc, D. Barredo, V. Lienhard, A. Browaeys, and T. Lahaye, Optical Control of the Resonant Dipole-Dipole Interaction between Rydberg Atoms, Phys. Rev. Lett. **119**, 053202 (2017).

[21] H. Levine, A. Keesling, A. Omran, H. Bernien, S. Schwartz, A. S. Zibrov, M. Endres, M. Greiner, V. Vuletić, and M. D. Lukin, High-Fidelity Control and Entanglement of Rydberg-Atom Qubits, Phys. Rev. Lett. **121**, 123603 (2018).

[22] C. Weitenberg, M. Endres, J. F. Sherson, M. Cheneau, P. Schauß, T. Fukuhara, I. Bloch, and S. Kuhr, Single-spin addressing in an atomic Mott insulator, Nature **471**, 319 (2011).

[23] Y. Wang, X. Zhang, T. A. Corcovilos, A. Kumar, and D. S. Weiss, Coherent Addressing of Individual Neutral Atoms in a 3D Optical Lattice, Phys. Rev. Lett. **115**, 043003 (2015).

[24] J. Wilson, S. Saskin, Y. Meng, S. Ma, R. Dilip, A. P. Burgers, and J. D. Thompson, Trapped arrays of alkaline earth Rydberg atoms in optical tweezers (2019), ArXiv:1912.08754.

[25] R. G. Cortiñas, M. Favier, B. Ravon, P. Méhaignerie, Y. Machu, J. M. Raimond, C. Sayrin, and M. Brune, Laser Trapping of Circular Rydberg Atoms, Phys. Rev. Lett. **124**, 123201 (2020).

[26] G. Lochead, D. Boddy, D. P. Sadler, C. S. Adams, and M. P. A. Jones, Number-resolved imaging of excited-state atoms using a scanning autoionization microscope, Phys. Rev. A **87**, 053409 (2013).

[27] S. Saskin, J. T. Wilson, B. Grinkemeyer, and J. D. Thompson, Narrow-Line Cooling and Imaging of Ytterbium Atoms in an Optical Tweezer Array, Phys. Rev. Lett. **122**, 143002 (2019).

[28] W. E. Cooke, T. F. Gallagher, S. A. Edelstein, and R. M. Hill, Doubly Excited Autoionizing Rydberg States of Sr, Phys. Rev. Lett. **40**, 178 (1978).

[29] R. M. Jopson, R. R. Freeman, W. E. Cooke, and J. Bokor, Electron Shake-Up in Two-Photon Excitation of Core Electrons to Rydberg Autoionizing States, Phys. Rev. Lett. **51**, 1640 (1983).

[30] T. F. Gallagher, Doubly excited states, J. Opt. Soc. Am. B **4**, 794 (1987).

[31] M. Saffman, I. I. Beterov, A. Dalal, E. J. Páez, and B. C. Sanders, Symmetric Rydberg controlled-*Z* gates with adiabatic pulses, Phys. Rev. A **101**, 062309 (2020).

[32] This is the total scattering rate including both Raman and Rayleigh scattering but we treat it as Raman scattering when $\Delta < \Delta_f$, the fine-structure splitting [48]. Given the required value of Δ derived below, this is self-consistent for gate errors $\epsilon \gtrsim 10^{-4}$ in Rb and Cs, given $\Delta_r/\Gamma \approx 10^6$ in these atoms.

[33] I. Zalivako, I. Semerikov, A. Borisenko, V. Smirnov, P. Vishnyakov, M. Aksenov, P. Sidorov, N. Kolachevsky, and K. Khabarova, Improved wavelength measurement of $2s_{1/2} \rightarrow 2p_{1/2}$ and $2d_{3/2} \rightarrow^3 [3/2]_{1/2}$ transitions in Yb^+, J. Russ. Laser Res. **40**, 375 (2019).

[34] R. Grimm, M. Weidemüller, and Y. B. Ovchinnikov, Optical dipole traps for neutral atoms, Adv. At. Mol. Opt. Phys. **42**, 95 (2000).

[35] S. Olmschenk, D. Hayes, D. N. Matsukevich, P. Maunz, D. L. Moehring, K. C. Younge, and C. Monroe, Measurement of the lifetime of the $6p^2P^o_{1/2}$ level of Yb^+, Phys. Rev. A **80**, 022502 (2009).

[36] We extract a scaled C_6 coefficient of $C_6 n^{-11} \approx -21^{+9}_{-7}$(a.u.) at $n = 50$ by determining the onset of blockaded Rabi oscillations versus the separation between atoms. The error is due to the uncertainty of our imaging-system magnification.

[37] N. H. Tran, R. Kachru, and T. F. Gallagher, Multistep laser excitation of barium: Apparent interferences due to overlap-integral variations, Phys. Rev. A **26**, 3016 (1982).

[38] D. Steck, Rubidium 87 D line data2003.

[39] S. Weber, C. Tresp, H. Menke, A. Urvoy, O. Firstenberg, H. P. Büchler, and S. Hofferberth, Calculation of Rydberg interaction potentials, J. Phys. B: At., Mol. Opt. Phys. **50**, 133001 (2017).

[40] S. Debnath, N. M. Linke, C. Figgatt, K. A. Landsman, K. Wright, and C. Monroe, Demonstration of a small programmable quantum computer with atomic qubits, Nature **536**, 63 (2016).

[41] N. H. Tran, P. Pillet, R. Kachru, and T. F. Gallagher, Multistep excitation of autoionizing Rydberg states, Phys. Rev. A **29**, 2640 (1984).

[42] N. Y. Du and C. H. Greene, Quantum defect analysis of HD photoionization, J. Chem. Phys. **85**, 5430 (1986).

[43] M. Aymar, C. H. Greene, and E. Luc-Koenig, Multichannel Rydberg spectroscopy of complex atoms, Rev. Mod. Phys. **68**, 1015 (1996).

[44] S. A. Bhatti, C. L. Cromer, and W. E. Cooke, Analysis of the Rydberg character of the $5d7d\,^1D_{21}$ state of barium, Phys. Rev. A **24**, 161 (1981).

[45] U. I. Safronova and M. S. Safronova, Third-order relativistic many-body calculations of energies, transition rates, hyperfine constants, and blackbody radiation shift in $^{171}Yb^+$, Phys. Rev. A **79**, 022512 (2009).

[46] U. Fano, Effects of configuration interaction on intensities and phase shifts, Phys. Rev. **124**, 1866 (1961).

[47] B. Shore, *The Theory of Coherent Atomic Excitation* (Wiley, New York, 1990).

[48] R. A. Cline, J. D. Miller, M. R. Matthews, and D. J. Heinzen, Spin relaxation of optically trapped atoms by light scattering, Opt. Lett. **19**, 207 (1994).

Correction: An inline equation in Sec. II, second paragraph, last sentence was missing a solidus and has been set right.